

Localized Surface Plasmon Enhanced All-Inorganic Perovskite Quantum Dot Light-Emitting Diodes Based on Coaxial Core/Shell Heterojunction Architecture

Zhifeng Shi, Ying Li, Sen Li, Xinjian Li,* Di Wu, Tingting Xu, Yongtao Tian, Yongsheng Chen, Yuantao Zhang, Baolin Zhang, Chongxin Shan,* and Guotong Du

This work presents a strategy of combining the concepts of localized surface plasmons (LSPs) and core/shell nanostructure configuration in a single perovskite light-emitting diode (PeLED) to address simultaneously the emission efficiency and stability issues facing current PeLEDs' challenges. Wide bandgap n-ZnO nanowires and p-NiO are employed as the carrier injectors, and also the bottom/upper protection layers to construct coaxial core/shell heterostructured CsPbBr₃ quantum dots LEDs. Through embedding plasmonic Au nanoparticles into the device and thickness optimization of the MgZnO spacer layer, an emission enhancement ratio of 1.55 is achieved. The best-performing plasmonic PeLED reaches up a luminance of 10 206 cd m⁻², an external quantum efficiency of ≈4.626%, and a current efficiency of 8.736 cd A⁻¹. The underlying mechanisms for electroluminescence enhancement are associated with the increased spontaneous emission rate and improved internal quantum efficiency induced by exciton–LSP coupling. More importantly, the proposed PeLEDs, even without encapsulation, present a substantially improved operation stability against water and oxygen degradation (30-day storage in air ambient, 85% humidity) compared with any previous reports. It is believed that the experimental results obtained will provide an effective strategy to enhance the performance of PeLEDs, which may push forward the application of such kind of LEDs.

The appealing properties of this class of semiconductor materials that enable advances in optoelectronic devices are high quantum efficiency, ambipolar charge transport, high light absorption coefficient, wavelength-tunable emission, and low-temperature processing technique. Compared to the intensive efforts on solar cell applications, the investigation of perovskites as light-emitters in energy-efficient light sources is relatively less intensive. Since the first demonstration of perovskite-based LEDs (PeLEDs) based on CsPbX₃ quantum dots (QDs) by Zeng and co-workers in 2015,^[8] the external quantum efficiencies (EQEs) of this kind of LEDs have exhibited a rapid rise over the past two years.^[9] However, there is still a lack of significant breakthroughs that could propel PeLEDs into the commercialization stage, although numerous efforts have been paid and perovskite processing approaches and device fabrication techniques have experienced continual innovations. On the one hand,


the inferior device performance is presumably due to that the emission from perovskite active layer is often hindered by the trap-mediated nonradiative recombination, and high internal quantum efficiency (IQE) could not be achieved until the defect states are filled with electrons in high pumping levels,

1. Introduction

Recently, the new-emerging metal halide perovskites have attracted great scientific attention in the fields of photovoltaics, photodetectors, light-emitting diodes (LEDs), and lasers.^[1–7]

Dr. Z. Shi, Dr. Y. Li, Dr. S. Li, Prof. X. Li, Dr. D. Wu, Dr. T. Xu, Dr. Y. Tian, Dr. Y. Chen, Prof. C. Shan
Key Laboratory of Materials Physics of Ministry of Education
Department of Physics
and Engineering
Zhengzhou University
Zhengzhou 450052, China
E-mail: lixj@zzu.edu.cn; cxshan@zzu.edu.cn
Prof. Y. Zhang, Prof. B. Zhang, Prof. G. Du
State Key Laboratory on Integrated Optoelectronics
College of Electronic Science and Engineering
Jilin University
Qianjin Street 2699, Changchun 130012, China

Prof. C. Shan
State Key Laboratory of Luminescence and Applications
Changchun Institute of Optics
Fine Mechanics and Physics
Chinese Academy of Sciences
Changchun 130033, China
Prof. G. Du
School of Physics and Optoelectronic Technology
Dalian University of Technology
Dalian 116023, China

 The ORCID identification number(s) for the author(s) of this article can be found under <https://doi.org/10.1002/adfm.201707031>.

DOI: 10.1002/adfm.201707031

thus reducing the carrier injection efficiency and radiative recombination probability. On the other hand, the operation stability of the PeLEDs, which is the main obstacle that hinders the reliable device operation and their potential applications drastically, remains highly unsatisfactory and needs to be improved. Therefore, in terms of EQE and stability, there are still many remaining challenges and potential breakthroughs for PeLEDs.

Currently, the coupling between excitons and localized surface plasmons (LSPs) by the incorporation of metallic nanostructures into LEDs is becoming one of the most promising approaches for the enhancement of device performance.^[10] In theory, as the energy of electron–hole pairs/excitons in a luminescent material is close to the SP's resonant energy, the energy shall be coupled into the SP mode and finally scattered/re-emitted into free space as radiation. Therefore, an extra recombination pathway is established, leading to an increased spontaneous radiation rate and improved emission performance. In optical pumping, LSP-enhanced photoluminescence (PL) has been demonstrated in various semiconductors, such as GaN, ZnO, and Si QDs.^[11–13] More recently, Yang and co-workers reported a sixfold enhancement of emission from $\text{CH}_3\text{NH}_3\text{PbI}_3$ by employing SPs in Au films and they considered that the PL enhancement is mainly resulted from the increased radiative recombination rate via LSP–exciton coupling.^[14] In electrical pumping, the introduction of LSPs has proven to be an effective strategy for improving the device efficiency, including the nitride-based and ZnO-based LEDs, as well as the organic LEDs.^[15–17] However, no report on plasmonic PeLEDs can be found up to now to the best of our knowledge. In addition to the LSPs effect, core/shell (CS) device configuration based on low-dimensional nanostructures has been recognized to be potentially ideal building blocks for nanoscale device assembly.^[18] Some features of the CS nanostructures would be favorable for an enhanced carrier recombination efficiency, such as increased junction area, enhanced carrier confinement, and effective surface passivation. Such CS configurations have been intensively studied by many researchers based on different semiconductor material systems. For instance, Liu et al. realized an enhanced PL emission from ZnO nanorods by using MgZnO as the coating layer to form coaxial CS ZnO/MgZnO nanostructures.^[12] Lieber and co-workers fabricated multiquantum-well CS nanowires (NWs) heterostructures based on well-defined III-nitride materials that enabled lasing over a broad wavelength range.^[19] In terms of PeLEDs, the design of a stacking multilayer structure based on CS configurations will provide more a chance for an enhanced operation stability except for an evaluated device emission efficiency, because the vulnerable perovskite active layer can be protected by the upper and bottom carrier injectors from exposure to air ambient. Based on the above analyses, we have reasons to consider that if the integration of SPs and CS nanostructures in a single PeLED could be developed, the significance and importance of this route will be self-evident because of the concurrent consideration of device emission efficiency and stability.

Following this line of thought, we designed and fabricated a LSP-enhanced coaxial CS heterostructured PeLEDs by embedding plasmonic Au nanoparticles (NPs) into the device structure. Wide bandgap metal oxide semiconductors, n-ZnO NWs

and p-NiO, were employed as the carrier injectors, and also the bottom/upper protection layers to construct CsPbBr_3 QDs LEDs. Through thickness optimization of the MgZnO spacer layer, an emission enhancement ratio of 1.55 has been achieved. The electroluminescence (EL) performance of the resulting PeLED is remarkable in terms of its high luminance (10206 cd m^{-2}), current efficiency (8.736 cd A^{-1}), and EQE (4.626%), as well as a substantially improved operation stability compared with any previous reports. It is believed that the experimental results obtained here will provide an effective strategy to enhance the performance of PeLEDs, which may push forward the application of such kind of LEDs.

2. Results and Discussions

Figure 1a shows the typical transmission electron microscopy (TEM) images of the as-synthesized CsPbBr_3 QDs, which are characterized by uniformly distributed monodisperse particles, with a tendency to show self-assembled agglomerates on the TEM grids. The histogram displayed in Figure S1 (Supporting Information) indicates a narrow size distribution of the CsPbBr_3 QDs with an average diameter of 9.0 nm. Note that the diameter of CsPbBr_3 QDs can be tuned in a range of 3.6–9.0 nm, corresponding to an emission range from 483 to 514 nm. From the high-resolution TEM image shown in Figure 1b, a well-defined crystalline structure can be obtained, and an interplanar distance of 2.96 Å corresponding to the (200) crystal planes of cubic CsPbBr_3 can be identified. The corresponding Fourier transformation (FFT) image shown in Figure 1c confirms the single-crystalline nature of the CsPbBr_3 QDs. The formation and structural characteristics of the CsPbBr_3 QDs were further confirmed by the X-ray diffraction (XRD) measurements. As shown in Figure 1d, the characteristic and dominant diffraction peaks at 15.13° , 21.52° , and 30.50° can be assigned to the (100), (110), and (200) planes of cubic CsPbBr_3 , matching well with their standard XRD pattern shown in the bottom panel (JCPDS No. 54–0752). Figure 1e presents the ultraviolet–visible absorption and PL spectra of the CsPbBr_3 QDs measured at room temperature (RT), and an obvious exciton absorption peak occurs at 503.5 nm. The PL spectrum of the CsPbBr_3 QDs features a highly symmetric emission peak at 514 nm with a narrow linewidth of 18.3 nm, showing an obvious blue-shift compared with the inorganic CsPbBr_3 thin films and microcrystals (Figure S2, Supporting Information). The small Stokes shift suggests that the PL emission of the CsPbBr_3 QDs originates from the bound exciton related recombination,^[20] and the excitonic emission behavior has been verified by performing the temperature-dependent and excitation power-dependent PL measurements (Figures S3 and S4, Supporting Information). In addition, the absorption spectrum of the Au NPs was also provided in Figure 1e. One can observe that the absorption spectrum sustains a broadband profile, offering a good overlapping degree with the PL emission of the CsPbBr_3 QDs, which implies the possible coupling resonance between the radiated light generated in the CsPbBr_3 QDs and the LSPs excited by the Au NPs. Thus, plasmonic PeLEDs with an enhanced emission performance are expected to be realized through a maximum coupling

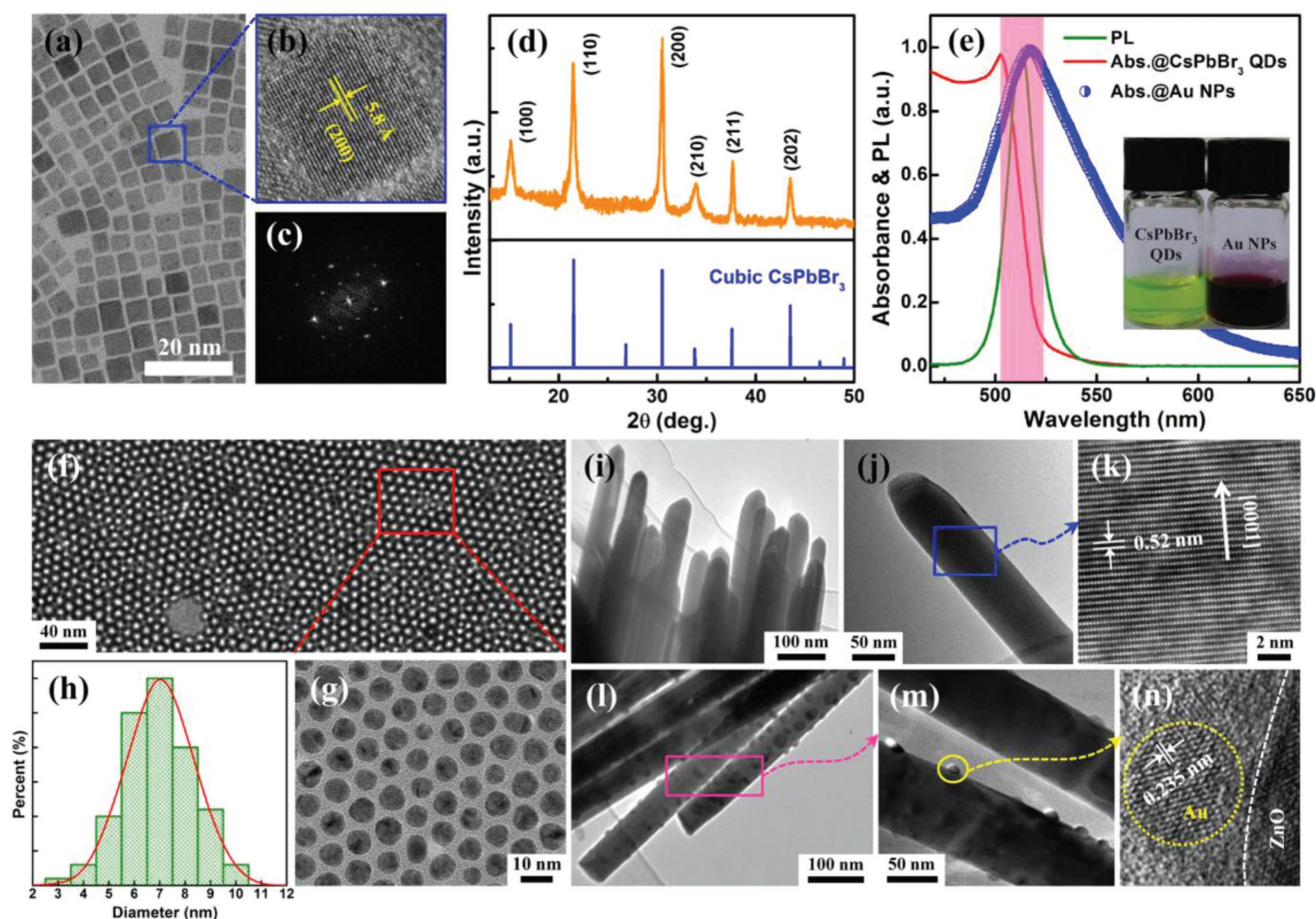


Figure 1. a) TEM images of the CsPbBr₃ QDs. b) High-resolution TEM image of the CsPbBr₃ QDs showing a characteristic lattice plane distance of ≈ 0.58 nm. c) FFT image corresponding to (b). d) XRD spectrum (top) of the CsPbBr₃ QDs film and standard XRD patterns (bottom) for the cubic CsPbBr₃. e) Absorption spectra (CsPbBr₃ QDs, Au NPs) and PL spectra (CsPbBr₃ QDs) measured at RT. The insets show the photographs of perovskite CsPbBr₃ QDs and Au NPs solutions. f,g) TEM images of the as-synthesized Au NPs. h) Histogram for the size distribution of the Au NPs. i,j) TEM images of as-grown ZnO NWs. k) High-resolution TEM image from the ZnO NW main body marked in (j). l,m) TEM images of Au NPs-decorated ZnO NWs. n) High-resolution TEM image showing the crystal lattice of Au NPs.

between the emission from CsPbBr₃ QDs and the SPs of Au NPs. The insets in Figure 1e display the photographs of the CsPbBr₃ QDs and Au NPs dispersed in hexane and methylbenzene solutions, respectively. In addition, TEM was used to characterize the topography of the Au NPs, which were dipped onto the copper grid and dried for measurement. As shown in Figure 1f,g, the as-synthesized Au NPs are spherical in shape and highly dispersed, which have an average diameter of 8.6 nm by statistical calculation (Figure 1h). For the preparation of plasmonic PeLEDs structured with coaxial NiO/CsPbBr₃ QDs/MgZnO/Au NPs/ZnO CS heterojunction architecture, the Au NPs were subjected to spin-coated on the surface of ZnO NWs. In order to investigate the structural characterizations of the produced Au NPs-decorated ZnO NWs in detail, TEM measurements were therefore performed. Figure 1i,j shows the low-magnification TEM images of as-grown ZnO NWs. It reveals that the ZnO NW has a quite smooth surface with a diameter of ≈ 100 nm. Figure 1k presents the high-resolution TEM image taken from the main body of the ZnO NW (marked by a blue square in Figure 1j), and well-resolved lattice fringes of the ZnO (0002) planes with an interplanar spacing

of ≈ 0.52 nm were observed, indicating that the as-grown ZnO NWs were single-crystalline with the preferred growth along the *c*-axis direction.^[21] After the Au NPs decoration, a rough geometrical configuration was produced, as seen in the corresponding TEM images shown in Figure 1l,m. From the selected areas marked by a pink square, one can clearly observe that the Au NPs were attached on the surface of the ZnO NWs separately, and a distinguished interface between the ZnO NW and surrounding Au NPs suggests the formation of Au NPs-decorated NW structure. Figure 1n exhibits the clear crystal lattice fringes of a single Au NP marked by a yellow circle in Figure 1m, and an interplanar distance of ≈ 0.235 nm agrees well with the lattice spacing of (111) planes of the cubic-structured Au phase, consistent with that of the Au bulk crystal (JCPDS No. 89–3697).^[22]

To prepare the multilayered heterostructure PeLEDs, five main processing procedures are involved in the following order: growth of well-aligned ZnO NWs, Au NPs decoration, MgZnO layer deposition, spin-coating of inorganic CsPbBr₃ QDs, and sputtering of NiO layer. To monitor the preparation process, we performed the scanning electron microscope (SEM)

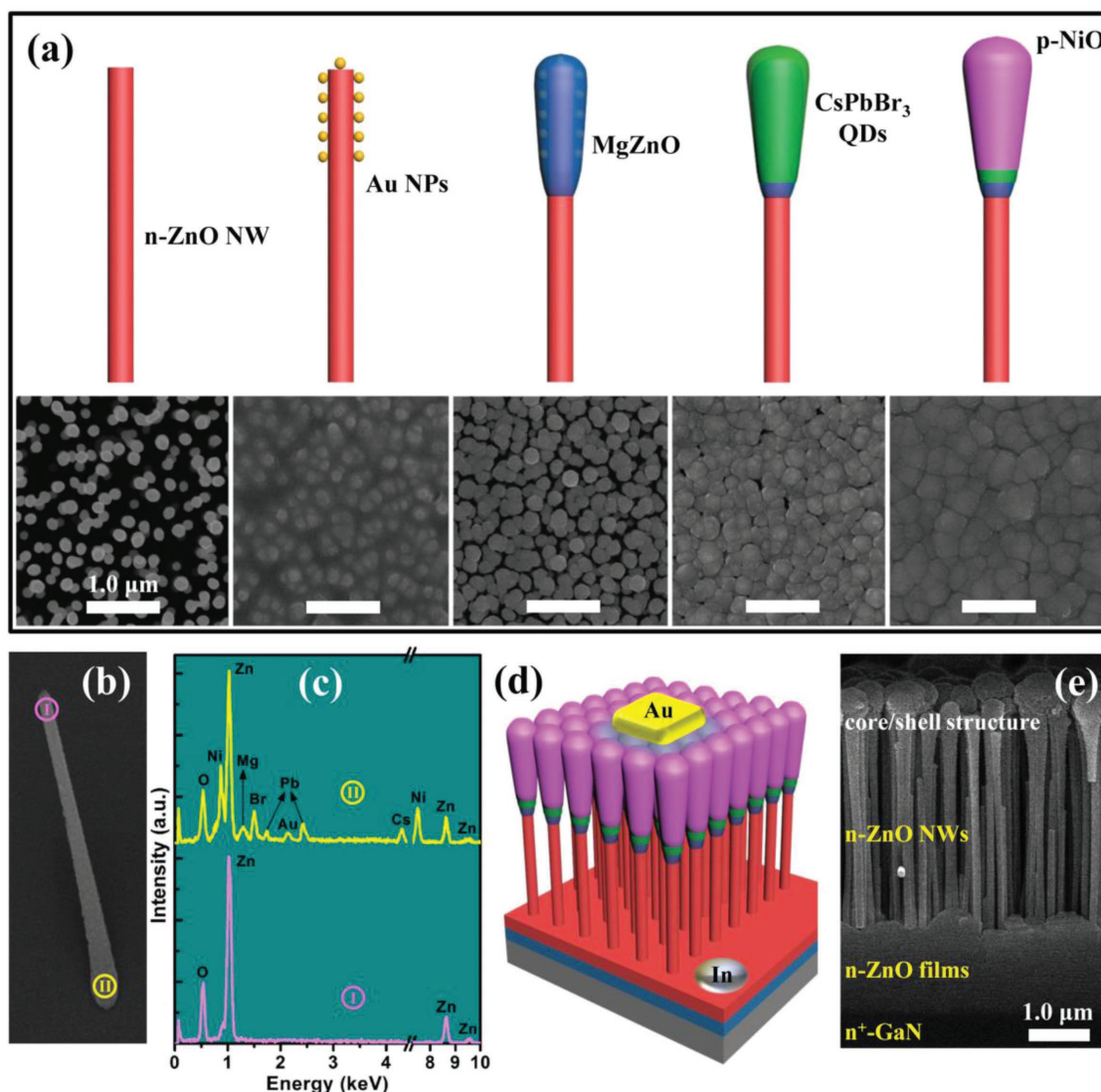


Figure 2. a) Processing procedures for the preparation of coaxial CS NW heterojunction architecture and the corresponding top-view SEM images after each step. b) Typical SEM image of a single NiO/CsPbBr₃ QDs/MgZnO/Au NPs/ZnO coaxial NW. c) EDS spectra acquired from different areas of a single coaxial CS NW marked in (b). d) Schematic diagram of the Au/p-NiO/CsPbBr₃ QDs/MgZnO/Au NPs/n-ZnO/n⁺-GaN heterostructure LED. e) Cross-sectional SEM image of the NiO/CsPbBr₃ QDs/MgZnO/Au NPs/ZnO coaxial NWs.

measurements after each step and the corresponding images are presented in **Figure 2a** (lower pane). By a comparative analysis of five SEM images, a regular variation of the morphological features can be observed: (1) the effective diameter of ZnO NWs at their heads is thickened gradually after Au NPs decoration and three layers (MgZnO, CsPbBr₃ QDs, and NiO) deposition, evolving into a round-cap-like structure finally, as clearly displayed in **Figure 2b**. (2) After three layers (MgZnO, CsPbBr₃ QDs, and NiO) deposition, the blank zones around the ZnO NWs were completely filled up, forming a densely packed morphology. (3) The deposition of MgZnO, CsPbBr₃ QDs, and NiO layers covers only the heads and side facets of ZnO NWs, with their thicknesses decreasing from the NW's top to its bottom gradually, forming coaxial NiO/CsPbBr₃ QDs/MgZnO/Au NPs/ZnO CS heterojunction architecture. The above coaxial coating configuration can be further confirmed by a typical SEM image

of a single NiO/CsPbBr₃ QDs/MgZnO/Au NPs/ZnO coaxial NW (**Figure 2b**) scratched from the underlying substrate. The upper pane of **Figure 2a** illustrates a schematic model demonstrating vividly the forming process of coaxial CS NW heterojunction architecture. The desired structural feature was further investigated by using the spot scanning energy-dispersive X-ray spectroscopy (EDS) measurements (seen in **Figure 2c**) on the bottom and head regions of vertical ZnO NWs, marked as "I" and "II" in **Figure 2b**. In region I, only Zn and O signals could be detected, while in region II, Ni, Mg, Br, Pb, Au, and Cs elements were identified except for the well-known compositions of Zn and O, indicating the formation of NiO/CsPbBr₃ QDs/MgZnO/Au NPs/ZnO CS NW structure and a decreasing shell layer thickness along the *c*-axis direction. Such morphology characteristics are significantly different from previously reported structures in PeLEDs that established with a

planar heterostructure,^[5,8] in which all functional layers are parallel in longitudinal direction. The effective coating of MgZnO, CsPbBr₃ QDs, and NiO around the ZnO NWs is believed to be favorable for increased heterojunction interface areas and a full protection of vulnerable perovskite active layer from exposure to air ambient, improving the carrier recombination efficiency and stabilizing the device operation. Figure 2d shows the schematic diagram of the studied device structure, and the configuration of NiO/CsPbBr₃ QDs/MgZnO/Au NPs/ZnO CS NWs heterostructure can be more clearly observed from the cross-sectional SEM image shown in Figure 2e.

In order to confirm the structural rationality of the fabricated PeLEDs and interpret the inherent carrier transport and recombination mechanisms, we illustrated the energy band alignment of the multilayered heterostructure based on the obtained ultraviolet–visible absorption data together with the ultraviolet photo-

electron spectroscopy (UPS) analysis. As shown in Figure 3a, the optical absorption spectra of CsPbBr₃ QDs, ZnO NWs, MgZnO, and NiO layers versus photon energy were drawn to determine the energy bandgap of these functional layers. As can be seen, linear extrapolation of the absorption edge gives out the optical band-gaps of 2.39 eV (CsPbBr₃ QDs), 3.30 eV (ZnO NWs), 3.61 eV (MgZnO), and 3.75 eV (NiO), respectively. In addition, the valence band maximum (VBM) positions of CsPbBr₃ QDs, ZnO NWs, MgZnO, and NiO layers were determined by the UPS results (Figure S5, Supporting Information), giving the data of −7.25, −7.45, −6.19, and −5.85 eV, respectively. By combining the band-gaps from ultraviolet–visible absorption spectra and VBM data from UPS spectra, the energy levels of four functional layers were calculated and the schematic band alignment was drawn with respect to the vacuum level (Figure 3b) assuming that there are no imperfections

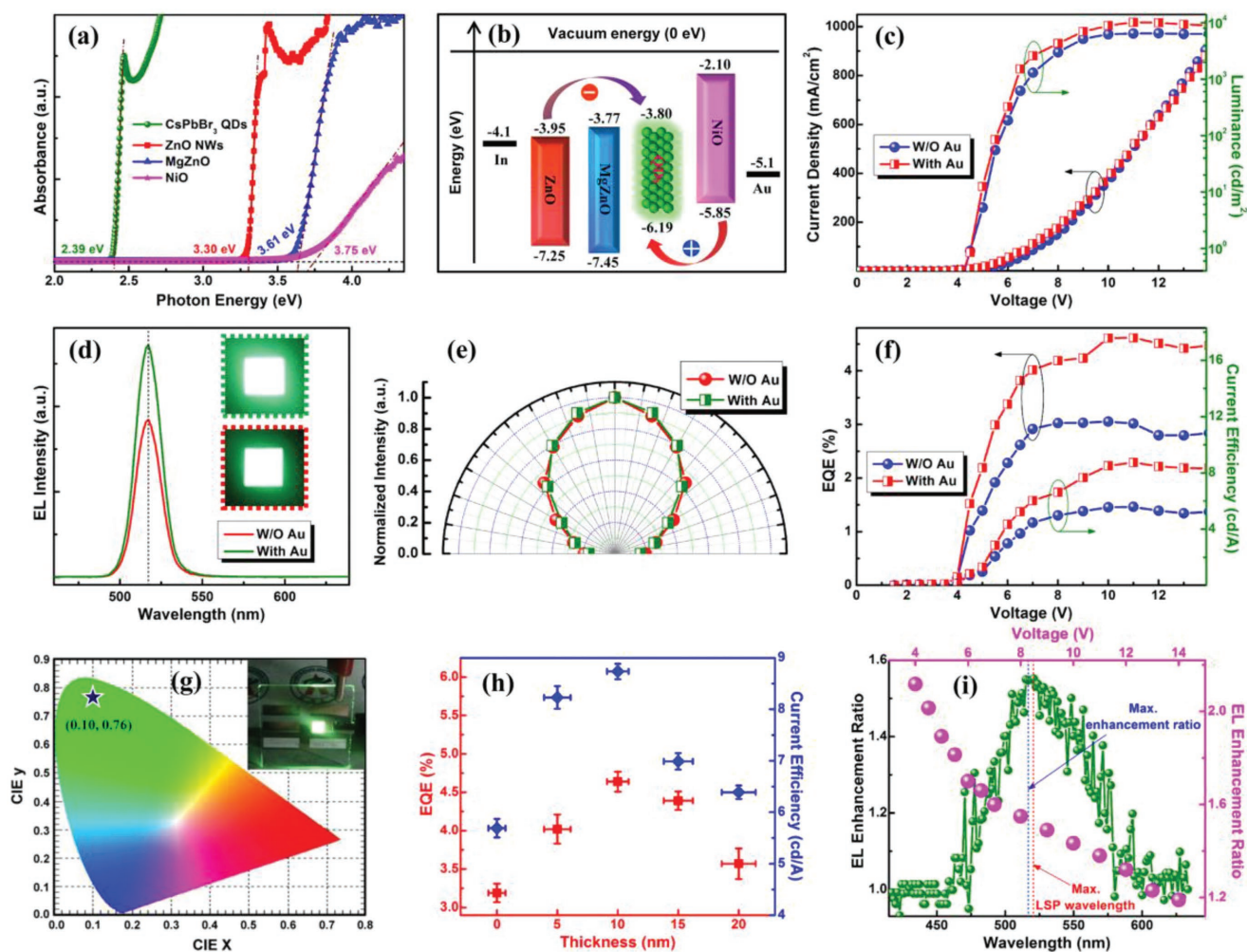


Figure 3. a) Absorption spectra of the CsPbBr₃ QDs, ZnO NWs, MgZnO, and NiO layers measured at RT. b) Simplified energy band alignment of the multilayered heterostructure showing the conduction and valence band energy levels with respect to the vacuum level. c) Current density and luminance of the PeLEDs with and without Au NPs decoration versus bias voltage. d) EL spectra of the plasmonic PeLED with Au NPs decoration and the reference device without Au NPs captured at 8.0 V. The insets present their corresponding emission photographs of an emitting unit (2 × 2 mm²). e) Angle-dependence of the EL intensity for the plasmonic PeLED and the reference device in a polar coordinate system. f) EQE and current efficiency of the plasmonic PeLED and reference device versus bias voltage. g) CIE coordinates of the plasmonic PeLED under a bias voltage of 8.0 V. The inset shows the photograph of a working device. h) EL enhancement ratio spectrum of the plasmonic PeLED as a function of wavelength and bias voltage. i) Device performance (EQE and current efficiency) with different thicknesses of MgZnO layer.

at the heterointerfaces. In the present case, the ZnO NWs could be deemed as an electron-providing layer and a transparent photon guider.^[23] The thin MgZnO layer with a n-type conductivity serves as the electron-injection and hole-blocking layer in virtue of its matched electron affinity with CsPbBr₃ and a relatively deep valence band energy level, as well as a spacer placed between Au NPs and emissive CsPbBr₃ QDs to avoid the emission quenching. The NiO layer with a p-type conductivity is employed as the hole-providing and electron-blocking layer because of its high ionization energy and low electron affinity. Although a low injection barrier for holes from NiO to CsPbBr₃ active layer still exists, the potential profile at the CsPbBr₃/NiO interface depends strongly on the magnitude of the applied bias. A slightly low external bias could effectively compensate the undesired energy barrier, thus holes injection or transport from NiO to CsPbBr₃ active layer takes effect, making the recombination of electrons and holes confined in the CsPbBr₃ layer possible.

As a comparison, a pristine PeLED without Au NPs decoration is also fabricated in parallel, and the device performances of two PeLEDs with and without Au NPs decoration are comparatively studied. Figure 3c plots the current density versus bias voltage (*J*-*V*) characteristics of two PeLEDs. The similar *J*-*V* curves and the same turn-on voltages of both two devices indicate that the Au NPs decoration does not provide any additional electrons which may contribute to the carrier injection. However, the luminance of the plasmonic PeLED was improved substantially compared with the controlled device without Au NPs. As shown in Figure 3c, the luminance increases from 6435 to 10 206 cd m⁻² at a current density of 490 mA cm⁻², producing an enhancement ratio of 58.6%. Figure 3d shows the typical EL spectra of the PeLEDs with and without Au NPs decoration acquired at 8.0 V, and the insets present their corresponding emission photographs of an emitting unit (2 × 2 mm²). One can observe that both two devices display intense green emission at ≈517.5 nm, and no any noticeable parasitic emission from carrier-providing layers was observed (Figure S6, Supporting Information). More importantly, the plasmonic PeLED demonstrates a 1.62-fold enhancement of spectrally integrated intensity in comparison with the reference device. By comparing the angle-dependence of the EL spectra for two PeLEDs (Figure 3e), almost identical features with increasing the view angles can be observed, ruling out the microcavity effect on the emission enhancement. Therefore, the large enhancement of EL intensity without any peak shift can be attributed to an efficient resonance coupling between the excitons in the QDs and LSPs in the Au NPs by a resonance energy matching since the emissive CsPbBr₃ QDs can fall in the local near-field of SPs induced by Au NPs (Figure 1e). In addition, other key device parameters, such as EQE and current efficiency of the PeLEDs, were also measured and plotted in Figure 3f as a function of bias voltage. By contrast, the plasmonic PeLED exhibits higher EQE and current efficiency at all comparable operating biases although two parameters of PeLEDs share the same changing trends. In detail, the best-performing plasmonic device reaches up an EQE of ≈4.626% and a current efficiency of 8.736 cd A⁻¹, about 52.9% and 56.5% enhancement in comparison with the controlled device without Au NPs decoration. Figure 3g shows the corresponding Commission International de l'Eclairage

(CIE) color coordinates (0.10, 0.72) of the plasmonic PeLED, and the inset displays a typical emission photograph of the working device from back side captured with a digital camera (at 8.0 V). To further understand the EL enhancement behavior observed above, the EL enhancement ratio, obtained by dividing the emission intensity of the plasmonic device by that of the device without Au NPs decoration, is calculated and plotted as a function of wavelength. As shown in Figure 3h, the most effective improvement of EL intensity occurs at 518.5 nm with a maximum enhancement ratio of ≈1.55, which matches well with the maximum LSP wavelength of Au NPs (Figure 1e), suggesting that the EL enhancement may arise from the mechanisms of LSP resonance coupling with excitons in CsPbBr₃ QDs. Besides, the EL enhancement ratio of the PeLEDs as a function of bias voltage was also plotted, and the ratio decreases rapidly then levels off at ≈1.19 as the bias voltage approach 14.0 V. This is a common feature for SPs-enhanced LEDs, and can be understood in terms of a screening effect of excess carriers by a high current injection, which will result in a weakening of LSP-exciton coupling.^[24]

Generally, the performance of SP-enhanced device shows a strong dependence on the distance of Au NPs and the emissive layer. In this study, the distance between the CsPbBr₃ QDs and the Au NPs is controlled by the thickness of MgZnO layer. As shown in Figure 3i, the dependence of the performance of the plasmonic PeLEDs on the thickness of MgZnO spacer is displayed by using EQE and current efficiency as the evaluation criterion. One can observe that the EQE (current efficiency) increases obviously from 3.192% (5.690 cd A⁻¹) to 4.626% (8.736 cd A⁻¹) as the thickness of MgZnO spacer is increased from 0 to 10 nm. While, further increasing the thickness of MgZnO layer only leads to a fast efficiency roll-off. It is generally accepted that the insertion of a spacer between Au NPs and emissive layer can effectively suppress the nonradiative Förster resonant energy transfer between Au and CsPbBr₃, favoring a LSP-induced field enhancement effect.^[25] However, it is also important to point out that the LSP is an evanescent wave that exponentially decays with distance from the Au NPs surface, and only excitons in CsPbBr₃ located within the near-field of the Au NPs could be coupled into the LSP mode. In addition, Liu et al. has proposed that a spacer layer with a proper thickness can reduce the metal dissipation of LSP energy and extend the near-field distribution range of the LSP.^[24] Therefore, considering the trade-off between the above two factors, it can be speculated that MgZnO layer with a thickness of 10 nm is an optimal distance to achieve the effective exciton-LSP resonance coupling which can over-ride the undesired quenching loss, leading to the maximum enhancement of the emission performance. To test it further, we calculated the penetration depth of the Au-LSP fringing field into MgZnO dielectric with a decay constant given by $Z = (\lambda/2\pi) \sqrt{(\epsilon'_1 - \epsilon'_2)/\epsilon'^2_2}$,^[26] in which ϵ'_1 and ϵ'_2 are the real parts of the dielectric constants of MgZnO (8.595) and Au (-10.92), and λ is the wavelength of light. The calculation yields a penetration depth (*Z*) of ≈32.9 nm for the emission (≈517 nm) of CsPbBr₃ active layer. Therefore, the optimal thickness of 10 nm for MgZnO spacer in our case is reasonable and convincing.

As mentioned above, the mechanisms of EL enhancement may be the exciton-LSP coupling. To support this argument,

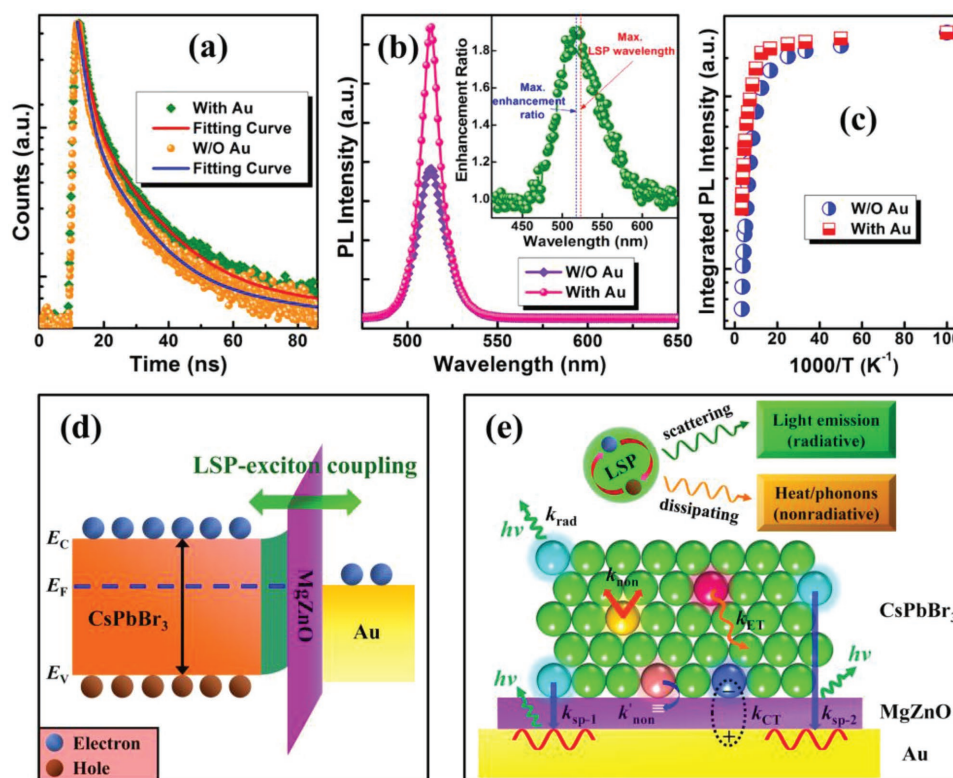


Figure 4. a) Time-resolved PL spectra of the CsPbBr₃ QDs samples with and without Au NPs decoration. b) PL spectra of the CsPbBr₃ QDs samples with and without Au NPs decoration measured at RT. c) Integrated PL intensity of the CsPbBr₃ QDs samples with and without Au NPs decoration as a function of reciprocal temperature from 10 to 300 K. d) Band alignment of the Au/MgZnO/CsPbBr₃ heterostructures. e) Detailed relaxation pathways of excitons in CsPbBr₃ QDs on Au plasmonic resonators with a MgZnO spacer layer.

time-resolved PL measurements of CsPbBr₃ QDs samples with and without Au NPs decoration were performed (Figure 4a). It has been reported that the coupling process between LSPs and excitons is much faster than the spontaneous recombination of excitons, and the exciton lifetime in SP-enhanced device should be reduced.^[24] As expected, the CsPbBr₃ QDs sample with Au NPs decoration shows a faster spontaneous emission rate than the reference sample. In detail, the decay time of CsPbBr₃ QDs sample is 7.72 ns, and it decreases to 4.56 ns with Au NPs decoration. Obviously, the shortened PL lifetime suggests that the LSPs provide an additional, high-rate recombination channel, and can be regarded as a strong evidence of exciton–LSP coupling. In theory, when the energy of excitons in CsPbBr₃ QDs is closer to the electron vibrational energy of the LSP in Au NPs, the energy of excitons can transfer to the LSPs and a new recombination path can be created. A Purcell enhancement factor (F_p) is therefore calculated to describe the increase in spontaneous recombination rate by the following equation^[27]

$$F_p = \tau_{PL} / \tau_{PL}^* = k_{PL}^* / k_{PL} \quad (1)$$

where τ_{PL} and τ_{PL}^* are the original and shortened effective PL lifetimes, respectively. Analogously, k_{PL} and k_{PL}^* represent the original and enhanced PL decay rates. A value of 1.69 for F_p is calculated consequently. As a matter of fact, the increase in recombination rate will also favor an improvement in IQE of the luminescent materials. In the present case, the IQE for

CsPbBr₃ QDs samples (η_{int}^*) with and (η_{int}) without Au NPs decoration can be expressed as^[11]

$$\eta_{int} = \frac{k_{rad}}{k_{rad} + k_{non}} \quad (2)$$

$$\eta_{int}^* = \frac{k_{rad} + C'_{ext} \cdot k_{sp}}{k_{rad} + k_{non} + k_{sp}} \quad (3)$$

in which k_{rad} and k_{non} are the radiative and nonradiative recombination rates of CsPbBr₃ QDs sample, k_{sp} is the exciton–LSP coupling rate, and C'_{ext} represents the possibility of photon extraction from the SP's energy and is generally supposed as $\approx 100\%$.^[11,28] Considering the fact that the exciton–LSP coupling rate k_{sp} is expected to be very fast compared to the k_{rad} and k_{non} , one can easily deduce that the η_{int}^* is larger than the η_{int} . Therefore, the EL enhancement obtained above is primarily attributed to the increase in IQE of the CsPbBr₃ QDs active layer as a result of the exciton–LSP resonant coupling, or says a new recombination path provided by the exciton–LSP coupling. Accordingly, the PL performance of the CsPbBr₃ QDs sample with Au NPs decoration measured at RT (Figure 4b) demonstrates an evident but logical improvement in comparison to the pristine CsPbBr₃ QDs sample, and a maximum PL enhancement ratio of ≈ 2.02 can be achieved at 516.5 nm, well

consistent with the observation in EL enhancement behavior. Note that the obtained PL enhancement ratio is larger than the EL enhancement ratio just because of the relatively more serious thermal effect in the EL process. Further, we performed the temperature-dependent PL measurements to get the experimental data of IQE for CsPbBr₃ QDs samples with and without Au NPs decoration. Figure 4c presents the Arrhenius plots of the integrated PL emission intensity of two samples, and one can clearly see that the CsPbBr₃ QDs sample with Au NPs decoration exhibits a relatively slower temperature quenching. The calculated IQE for Au NPs decorated sample is about 49.3% assuming that the radiative recombination efficiency at 10 K is 100%, and that for pristine CsPbBr₃ QDs sample is only 26.5%. The nearly twofold improvement in IQE is another evidence of exciton–LSP coupling. Moreover, the C'_{ext} was also estimated based on the above equations and the obtained experimental data. At the low-temperature region (≤ 30 K), the value of C'_{ext} approaches 100%, and it decreases gradually with increasing temperature. At 300 K, a rather high value of $\approx 67\%$ can be still achieved, which suggests that most of the LSP's energy was converted into the photon energy even at RT, and is also a direct evidence for LSP-enhanced emission performance.

To better understand the exciton–LSP coupling and light extraction processes, band alignment diagram of the Au NPs-decorated CsPbBr₃ QDs in contact with MgZnO spacer was drawn, and the elementary relaxation pathways of excitons on Au plasmonic resonators were also summarized and presented vividly. Figure 4d shows the energy band diagram of the Au/MgZnO/CsPbBr₃ heterostructures, in which a type-I band alignment at the CsPbBr₃/MgZnO interface was established. The 10 nm thick MgZnO spacer is sufficiently thick to effectively prevent the nonradiative energy transfer between perovskite active layer and Au NPs, and it is thin enough to retain effective exciton–LSP coupling. Besides, the MgZnO spacer can also serve as a dielectric layer to passivate the surface states of CsPbBr₃ QDs, and thus reduces the potential variation and narrows the depletion region near the perovskite surface, which in turn enhances the overlap of wave functions of electrons and holes and the carrier recombination efficiency. The detailed recombination mechanisms or relaxation pathways of excitons in CsPbBr₃ QDs can be found in Figure 4e. It is generally accepted that the excitons generated by electrical pumping are primarily terminated by radiative (k_{rad}), nonradiative (k_{non}), and exciton–LSP coupling (k_{sp}) processes. In terms of the exciton–LSP coupling process, two possible contributions or pathways should be considered. In our case, the CsPbBr₃ QDs active layer has a thickness of about 40 nm, not a monolayer or few-layer structure. For the excitons generated in the bottom region of perovskite layer (perovskite/MgZnO interface), a direct coupling of excitons to Au LSP mode ($k_{\text{sp-1}}$) can be expected. However, if the excitons are formed away from the perovskite/MgZnO interface or at the upper region of the perovskite layer, the direct long-range coupling to LSP mode ($k_{\text{sp-2}}$) will be more or less restricted by the bottom CsPbBr₃ QDs. In this case, the excitons view the bottom lying CsPbBr₃ QDs as simple dielectric layer as in the same manner as the MgZnO spacer. Since it would take more time for excitons to reach the perovskite/MgZnO interface, a multiple downward energy transfer among adjacent QDs (k_{ET}) will take place. Besides, the excitons existed

at the perovskite/MgZnO interface would partly undergo the interfacial nonradiative relaxation due to the electronic states of MgZnO, which is denoted as k'_{non} . Last but not least, the interfacial charge transfer or tunneling to the metal (k_{CT}) would also happen inevitably, which decays exponentially with increasing MgZnO spacer thickness. The rate constant for charge transfer or tunneling process can be described by an exponential decay function^[25]

$$k_{\text{CT}} = k'_{\text{CT}} \exp\left(-\frac{d}{d_{\text{CT}}}\right) \quad (4)$$

where k'_{CT} is the rate constant when the CsPbBr₃ QDs are directly on the metal layer, d_{CT} is the tunneling distance, and d is the thickness of MgZnO spacer. Theoretically, the charge transfer or tunneling process will spontaneously occur once the generated excitons reach the perovskite/MgZnO interface.

Despite the substantial improvement of EL performance by Au NPs decoration, the long-term operation stability of the plasmonic PeLEDs in a continuous mode remains a challenge. In our work, the preliminary stability study of the plasmonic PeLEDs without encapsulation was carried out using the “single point versus time” measurements under ambient conditions (25 °C, 20–30% humidity), in which a constant bias voltage of 8.0 V was applied and the emission intensity was recorded in real time. As shown in Figure 5a, the plasmonic PeLED could operate continuously for 60 h with an emission decay of $\approx 14.3\%$, greatly superior to other previously reported PeLEDs constructed with MAPbBr₃ or CsPbBr₃ emissive layer (Table 1).^[5,29–39] Although a pronounced gap still exists as compared with the nitride LEDs and traditional CdSe/ZnS QDs LEDs,^[15,40] a huge progress on operation stability opens up enormous opportunities for future practical applications. So what are the reasons for the substantially improved stability even operated at air ambient and without encapsulation. By analyzing our device structure and experimental results, four possible reasons are summarized and listed as follows: (1) In our case, the PeLEDs were designed based on vertically aligned and highly uniform one-dimensional (1D) ZnO NWs arrays, which are featured with a large surface–volume ratio, implying that the heat generated in the emitting unit could be easily released. (2) The CS structured device architecture differs from the traditional planar structure, in which 1D ZnO NWs core can be regarded as a promising photon guider to increase the light extraction efficiency of the PeLEDs considering the feasible waveguiding properties of NWs;^[41,42] thus the reabsorption effect of photons, which then again accounts for the heating problem, could be effectively suppressed because the emitted light is more likely to escape from the device. (3) The desirable coaxial CS heterojunction architecture, with a special geometric morphology, provides more a chance for a fully protection of vulnerable perovskite active layer from exposure to air ambient than the standard planar structure, thereby stabilizing the device operation. (4) Metal oxide semiconductors, ZnO and NiO, were employed as the carrier-providing layers in such PeLEDs, and their superior stability against degradation by the exposure to atmosphere for a long time and inherent material stability make them attractive candidates for device preparations.^[43,44] In addition, an interesting observation is that the

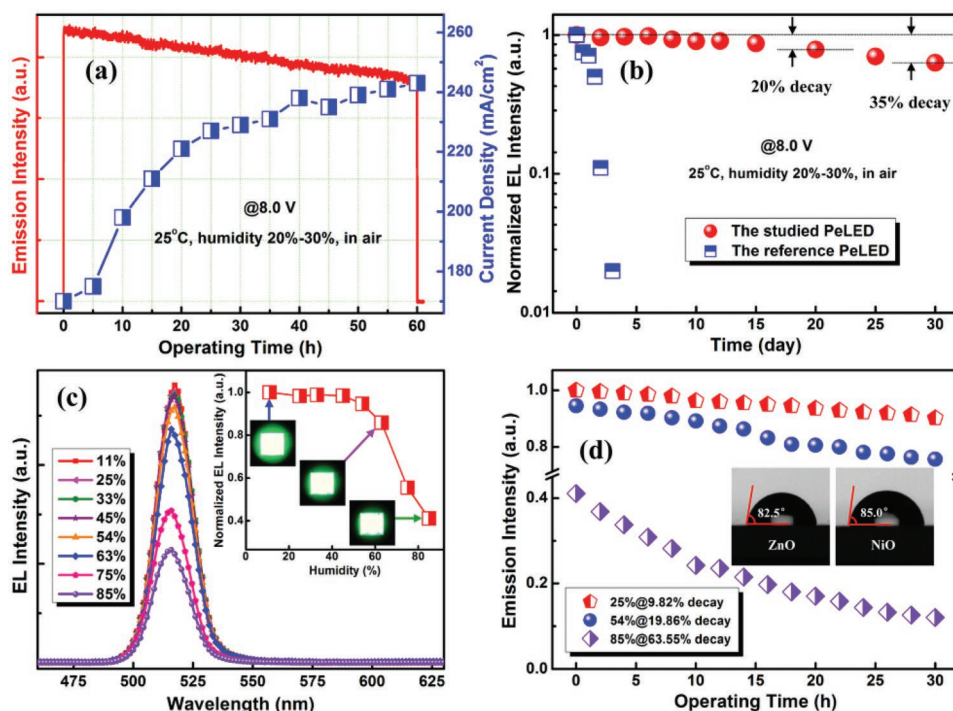


Figure 5. a) Time dependence (60 h) of the emission intensity and current density of the plasmonic PeLED at a fixed bias voltage of 8.0 V. b) Device performance of the plasmonic PeLED and the reference PeLED as a function of storage time in an ambient environment. c) Humidity-dependent EL spectra of the plasmonic PeLED at a bias voltage of 8.0 V. The inset shows the dependence of the integrated EL intensity versus ambient humidity and the corresponding photographs of an emitting unit. d) Emission decays of the plasmonic PeLED after different running periods under different humidity conditions. The insets show the water contact angles of ZnO and NiO layers deposited on n⁺-GaN/c-Al₂O₃ substrates.

current density of the plasmonic PeLED as a fixed bias voltage of 8.0 V rises slightly with running time. As there is no chemical reaction or phase transition in the device, we herein propose that the increasing current density is presumably because of the interface contact improvement (MgZnO/CsPbBr₃, CsPbBr₃/NiO) or perovskite crystalline layer annealing caused

by the inevitable joule heating.^[45] Besides, some recent studies recognized that the electrical-field-induced ion migration could destroy the lattice of perovskites, generating halide vacancy defects and forming charge-accumulated interfaces.^[46,47] Therefore, for a long-term operation of PeLEDs, the perovskite layer would become more conducting over running time. Note that

Table 1. Summary of the device performances of the PeLEDs.

Emission materials	EL λ_{max} ^{a)} [nm]	Max. Lu ^{b)} [cd m ⁻²]	Max. CE ^{c)} [cd A ⁻¹]	Max. EQE [%]	t_R ^{d)} [min]	Emission decay	Ref.
MAPbBr ₃ films	530	4064	0.74	0.165	4	67%	[29]
MAPbBr ₃ films	535	1.8	0.013	–	48	58%	[30]
MAPbBr ₃ films	533	186	0.12	0.065	4	75%	[31]
MAPbBr ₃ films	528	8794	5.1	–	3	90%	[32]
MAPbBr ₃ QDs	520	3515	11.49	3.8	0.5	50%	[33]
MAPbBr ₃ QDs	520	2398	–	1.20	600	90%	[34]
CsPbBr ₃ films	527	407	0.035	0.008	20	50%	[35]
CsPbBr ₃ films	524	7276	0.57	0.15	100	40%	[36]
CsPbBr ₃ films	530	>15 000	23	7.3	275	58%	[37]
CsPbBr ₃ QDs	516	1377	0.19	0.06	10	50%	[38]
CsPbBr ₃ QDs	516	3091	0.57	0.11	105	30%	[39]
CsPbBr ₃ QDs	522	3809	2.25	2.39	600	20%	[5]
CsPbBr ₃ QDs	518	10 206	8.73	4.63	3600	14.3%	This work

^{a)} λ_{max} : Peak position; ^{b)}Lu: Luminance; ^{c)}CE: Current efficiency; ^{d)} t_R : Running time.

such a changing process is irreversible, even if the resulting device is cooled down.

As further verification of the stability of the studied PeLEDs, we monitored the decay of the emission intensity of the unencapsulated device at different storage time under ambient conditions (25 °C, 20–30% humidity). As shown in Figure 5b, the majority of the original device performance was retained for up to 30 d, convincingly confirming the resistance of the proposed coaxial CS heterostructured PeLEDs against oxygen and water degradation. Specifically, a 20-day storage of the PeLED produced an emission decay of ≈20% and after 30-day storage the emission decay increased to 35%. Even so, the stability of the plasmonic PeLED is still superior to other previously reported planar PeLEDs constructed with organic electron-providing and/or hole-providing layers.^[8,9,29,30,32–38,48] For instance, a single replacement of NiO with conducting poly(3,4-ethylenedioxythiophen) polystyrenesulfonate would result in a distinct device performance. As shown in Figure 5b, the reference PeLED experiences a continual and fast degradation with time in open air, and almost fully decays after three days. This observation not only verifies the positive roles of inorganic carrier injectors on the improvement in device stability, but also highlights the essential advantages of coaxial CS heterojunction architecture for enhanced device performance.

In real life, the functional LEDs have to work outdoors with an unconstant humidity condition. Therefore, we also performed the aggressive humidity tests to further evaluate the operation stability of the studied PeLEDs in different humidity atmospheres (11–85% humidity). As shown in Figure 5c, a regular change on the EL spectra was found with the successive increase in humidity at a fixed bias voltage of 8.0 V. The EL intensity of the PeLEDs reduces monotonously with increasing humidity although the central positions of the emission peaks remain unchanged. However, the observed emission degradation with humidity is not represented as linear duration. The inset of Figure 5c shows the dependence of the integrated EL intensity versus ambient humidity. One can see that at the initial humidity-rise period from 11% to 54%, the EL intensity is slightly changed with an imperceptible reduction of ≈4.89%. While, the emission decay extent shows an increasing trend as the humidity is increased further. In 63% humidity, the integrated EL intensity decreases to 86% and in 85% humidity, about 43% of the original emission remains. The insets of Figure 5c also illustrate the corresponding photographs of an emitting unit of the PeLED acquired at different humidity, and a weakening trend on the emission intensity can be distinguished. The above experiments indicate a high humidity tolerance of the proposed PeLEDs, and are also evident of the rational device design with an all-inorganic coaxial CS heterojunction architecture. For a better understanding on the humidity tolerance of the plasmonic PeLEDs, we further performed the long-term operation test in low-/high-humidity ambient environment. As shown in Figure 5d, in 25% humidity, only a ≈9.82% emission decay was observed after 30 h running period. While, the emission decays at 54% and 85% humidity increase to ≈19.86% and ≈63.55%, respectively. Despite this, the current results obtained are a considerable advance toward the realization of practical PeLEDs, facilitating the existing applications and suggesting new potentials in other fields. In

our opinion, the high humidity tolerance of the studied PeLEDs benefits from the well-designed all-inorganic coaxial CS heterostructures. On the one hand, it has been generally accepted that the inorganic metal-oxide semiconductors (ZnO and NiO) could function as the moisture barriers that prevent water from penetrating into the sandwiched perovskite emitters.^[39,44] The insets of Figure 5d show the measured water contact angles of ZnO and NiO layers deposited on n⁺-GaN/c-Al₂O₃ substrates, and relatively large contact angles of 82.5° and 85.0° suggest weak hydrophilicity of carrier injectors. On the other hand, the coaxial CS NW heterostructure in our case can be deemed as an ideal building block for stabilizing the device operation, and the vulnerable CsPbBr₃ QDs emissive layer was fully protected by the upper and bottom carrier injectors. Thus, the resulting PeLEDs, even without encapsulation, can be efficiently sustained in high-humidity atmospheres, indicating desired compatibility for practical applications under harsh conditions.

3. Conclusions

In conclusion, we have successfully demonstrated the LSP-enhanced coaxial CS heterostructured PeLEDs by embedding plasmonic Au NPs into the device structure. Through thickness optimization of the MgZnO spacer layer, an emission enhancement ratio of 1.55 is achieved. The best-performing plasmonic PeLED reaches up a luminance of 10 206 cd m⁻², an EQE of ≈4.626%, and a current efficiency of 8.736 cd A⁻¹. The underlying mechanisms for EL enhancement is associated with the increased rate of spontaneous emission and improved IQE induced by exciton–LSP coupling. More importantly, the proposed PeLEDs, even without encapsulation, present a remarkable operation stability against water and oxygen degradation after 30-day storage in air ambient, and the EL emission can be efficiently sustained in a high humidity of 85%. The mechanisms of the excellent operation stability have been discussed on the basis of the coaxial CS heterojunction configuration and the hydrophilic properties of inorganic carrier injectors. It is reasonably believed that the results obtained provide a novel strategy for the design and development of high-efficiency and stable PeLEDs by combining the concepts of coaxial CS configuration and LSPs.

Supporting Information

Supporting Information is available from the Wiley Online Library or from the author.

Acknowledgements

The authors thank Dr. Peinan Ni for useful discussions on device performance. This work was supported by the National Natural Science Foundation of China (Grant Nos. 11774318, 11604302, 61176044, and 11504331), the China Postdoctoral Science Foundation (Grant Nos. 2015M582193 and 2017T100535), the Science and Technology Research Project of Henan Province (Grant No. 162300410229), the Postdoctoral Research Sponsorship in Henan Province (Grant No. 2015008), the Outstanding Young Talent Research Fund of Zhengzhou University (Grant No. 1521317001), and the Startup Research Fund of Zhengzhou University (Grant No. 1512317003).

Conflict of Interest

The authors declare no conflict of interest.

Keywords

core/shell architectures, light-emitting diodes, perovskite, plasmonic nanoparticles, stability

Received: December 4, 2017

Revised: February 6, 2018

Published online: February 28, 2018

- [1] W. S. Yang, J. H. Noh, N. J. Jeon, Y. C. Kim, S. Ryu, J. Seo, S. I. Seok, *Science* **2015**, *348*, 1234.
- [2] D. P. McMeekin, G. Sadoughi, W. Rehman, G. E. Eperon, M. Saliba, M. T. Hörlantner, A. Haghighirad, N. Sakai, L. Korte, B. Rech, M. B. Johnston, L. M. Herz, H. J. Snaith, *Science* **2016**, *351*, 151.
- [3] X. Wu, P. Liu, L. Ma, Q. Zhou, Y. Chen, J. Lu, S. Yang, *Sol. Energy Mater. Sol. Cell.* **2016**, *152*, 111.
- [4] J. P. Wang, N. Wang, Y. Z. Jin, J. J. Si, Z. K. Tan, H. Du, L. Cheng, X. Dai, S. Bai, H. P. He, Z. Z. Ye, M. L. Lai, R. H. Friend, W. Huang, *Adv. Mater.* **2015**, *27*, 2311.
- [5] Z. Shi, Y. Li, Y. T. Zhang, Y. S. Chen, X. J. Li, D. Wu, T. T. Xu, C. X. Shan, G. T. Du, *Nano Lett.* **2017**, *17*, 313.
- [6] S. Yakunin, L. Protesescu, F. Krieg, M. I. Bodnarchuk, G. Nedelcu, M. Humer, G. D. Luca, M. Fiebig, W. Heiss, M. V. Kovalenko, *Nat. Commun.* **2015**, *6*, 8056.
- [7] W. Zhang, L. Peng, J. Liu, A. Tang, J. S. Hu, J. N. Yao, Y. S. Zhao, *Adv. Mater.* **2016**, *28*, 4040.
- [8] J. Z. Song, J. H. Li, X. M. Li, L. M. Xu, Y. H. Dong, H. B. Zeng, *Adv. Mater.* **2015**, *27*, 7162.
- [9] S. A. Veldhuis, P. P. Boix, N. Yantara, M. Li, T. C. Sum, N. Mathews, S. G. Mhaisalkar, *Adv. Mater.* **2016**, *28*, 6804.
- [10] X. Yang, P. L. H. Martine, C. Dang, E. Mutlugun, K. Zhang, H. V. Demir, X. W. Sun, *Adv. Opt. Mater.* **2015**, *3*, 1439.
- [11] K. Okamoto, I. Niki, A. Shvartser, Y. Narukawa, T. Mukai, A. Scherer, *Nat. Mater.* **2004**, *3*, 601.
- [12] W. Z. Liu, Y. Liang, H. Y. Xu, L. Wang, X. Zhang, Y. C. Liu, S. Hark, *J. Phys. Chem. C* **2010**, *114*, 16148.
- [13] C. A. Lin, D. S. Tsai, C. Y. Chen, J. H. He, *Nanoscale* **2011**, *3*, 1195.
- [14] L. B. Xu, Y. P. Qiang, K. Xiao, Y. H. Zhang, J. S. Xie, C. Cui, P. Lin, P. Wang, X. G. Yu, F. M. Wu, D. R. Yang, *Appl. Phys. Lett.* **2017**, *110*, 233113.
- [15] M. K. Kwon, J. Y. Kim, B. H. Kim, I. K. Park, C. Y. Cho, C. C. Byeon, S. J. Park, *Adv. Mater.* **2008**, *20*, 1257.
- [16] P. N. Ni, C. Shan, S. P. Wang, Y. J. Lu, B. H. Li, D. Z. Shen, *Appl. Phys. Lett.* **2015**, *107*, 231108.
- [17] K. Y. Yang, K. C. Choi, C. W. Ahn, *Appl. Phys. Lett.* **2009**, *94*, 173301.
- [18] W. Liu, H. Xu, J. Ma, C. Liu, Y. Liu, Y. Liu, *Appl. Phys. Lett.* **2012**, *100*, 203101.
- [19] F. Qian, S. Gradecak, H. G. Park, Y. Dong, Y. Ding, Z. L. Wang, C. M. Lieber, *Nat. Mater.* **2008**, *7*, 701.
- [20] X. M. Li, Y. Wu, S. L. Zhang, B. Cai, Y. Gu, J. Z. Song, H. B. Zeng, *Adv. Funct. Mater.* **2016**, *26*, 2435.
- [21] Z. F. Shi, T. T. Xu, D. Wu, Y. Zhang, B. L. Zhang, Y. Tian, X. Li, G. T. Du, *Nanoscale* **2016**, *8*, 9997.
- [22] Y. Lin, C. X. Xu, J. T. Li, G. Y. Zhu, X. Y. Xu, J. Dai, B. P. Wang, *Adv. Opt. Mater.* **2013**, *1*, 940.
- [23] Y. Lu, Z. Shi, C. Shan, D. Shen, *Chin. Phys. B* **2017**, *26*, 047703.
- [24] W. Z. Liu, H. Y. Xu, L. X. Zhang, C. Zhang, J. G. Ma, J. N. Wang, Y. C. Liu, *Appl. Phys. Lett.* **2012**, *101*, 142101.
- [25] T. Shin, K. S. Cho, D. J. Yun, J. Kim, X. S. Li, E. S. Moon, C. W. Baik, S. I. Kim, M. Kim, J. H. Choi, G. S. Park, J. K. Shin, S. Hwang, T. S. Jung, *Sci. Rep.* **2016**, *6*, 26204.
- [26] B. J. Lawrie, R. F. H. Jr, R. Mu, *Opt. Express* **2009**, *17*, 2565.
- [27] K. W. Liu, Y. D. Tang, C. X. Cong, T. C. Sum, A. C. H. Huan, Z. X. Shen, L. Wang, F. Y. Jiang, X. W. Sun, H. D. Sun, *Appl. Phys. Lett.* **2009**, *94*, 151102.
- [28] S. G. Zhang, X. W. Zhang, Z. G. Yin, J. X. Wang, J. J. Dong, H. L. Gao, F. T. Si, S. S. Sun, Y. Tao, *Appl. Phys. Lett.* **2011**, *99*, 181116.
- [29] J. Q. Li, S. G. R. Bade, X. Shan, Z. B. Yu, *Adv. Mater.* **2015**, *27*, 5196.
- [30] M. F. Aygüler, M. D. Weber, B. M. D. Puscher, D. D. Medina, P. Docampo, R. D. Costa, *J. Phys. Chem. C* **2015**, *119*, 12047.
- [31] Z. Shi, X. Sun, D. Wu, T. Xu, S. Zhuang, Y. Tian, X. Li, G. Du, *Nanoscale* **2016**, *8*, 10035.
- [32] Z. B. Wang, T. Cheng, F. Z. Wang, S. Y. Dai, Z. Tan, *Small* **2016**, *12*, 4412.
- [33] J. Xing, F. Yan, Y. Zhao, S. Chen, H. K. Yu, Q. Zhang, R. Zeng, H. V. Demir, X. W. Sun, A. Huan, Q. H. Xiong, *ACS Nano* **2016**, *10*, 6623.
- [34] W. Deng, X. Xu, X. J. Zhang, Y. D. Zhang, X. C. Jin, L. Wang, S. T. Lee, J. S. Jie, *Adv. Funct. Mater.* **2016**, *26*, 4797.
- [35] N. Yantara, S. Bhaumik, F. Yan, D. Sabba, H. A. Dewi, N. Mathews, P. P. Boix, H. V. Demir, S. Mhaisalkar, *J. Phys. Chem. Lett.* **2015**, *6*, 4360.
- [36] Z. H. Wei, A. Perumal, R. Su, S. Sushant, J. Xing, Q. Zhang, S. T. Tan, H. V. Demir, Q. H. Xiong, *Nanoscale* **2016**, *8*, 18021.
- [37] H. P. Kim, J. Kim, B. S. Kim, H. M. Kim, J. Kim, A. R. B. M. Yusoff, J. Jang, M. K. Nazeeruddin, *Adv. Opt. Mater.* **2017**, *27*, 4013.
- [38] X. Y. Zhang, H. Lin, H. Huang, C. Reckmeier, Y. Zhang, W. C. H. Choy, A. L. Rogach, *Nano Lett.* **2016**, *16*, 1415.
- [39] Q. S. Shan, J. H. Li, J. Z. Song, Y. S. Zou, L. M. Xu, J. Xue, Y. H. Dong, C. X. Huo, J. W. Chen, B. N. Han, H. B. Zeng, *J. Mater. Chem. C* **2017**, *5*, 4565.
- [40] H. B. Shen, W. Cao, N. T. Shewmon, C. Yang, L. S. Li, J. Xue, *Nano Lett.* **2015**, *15*, 1211.
- [41] W. Liu, H. Xu, C. Wang, L. Zhang, C. Zhang, S. Sun, J. Ma, X. Zhang, J. Wang, Y. Liu, *Nanoscale* **2013**, *5*, 8634.
- [42] Y. Lu, C. Shan, Z. Zhou, Y. Wang, B. Li, J. Qin, H. Ma, X. Jia, Z. Chen, D. Shen, *Optica* **2015**, *2*, 558.
- [43] F. Fu, T. Feurer, T. P. Weiss, S. Pisoni, E. Avancini, C. Andres, S. Buecheler, A. N. Tiwari, *Nat. Energy* **2016**, *2*, 16190.
- [44] J. B. You, L. Meng, T. B. Song, T. F. Guo, Y. Yang, W. H. Chang, Z. Hong, H. Chen, H. Zhou, Q. Chen, Y. S. Chen, N. D. Marco, Y. Yang, *Nat. Nanotechnol.* **2016**, *11*, 75.
- [45] Z. Xiao, R. A. Kerner, L. F. Zhao, N. L. Tran, K. M. Lee, T. W. Koh, G. D. Scholes, B. P. Rand, *Nat. Photonics* **2017**, *11*, 108.
- [46] Y. Yuan, J. Huang, *Acc. Chem. Res.* **2016**, *49*, 286.
- [47] N. Ahn, K. Kwak, M. S. Jang, H. Yoon, B. Y. Lee, J. Lee, P. V. Pikhitsa, J. Byun, M. Choi, *Nat. Commun.* **2016**, *7*, 13422.
- [48] Y. H. Kim, H. Cho, T. W. Lee, *Proc. Natl. Acad. Sci. USA* **2016**, *113*, 11694.